Available online at www.sciencedirect.com
ScienceDirect
Trans. Nonferrous Met. Soc. China 28(2018) 1530−1537

Transactions of
Nonferrous Metals
Society of China
www.tnmsc.cn

Microstructural characterization of Inconel 718 alloy after pulsed laser surface treatment at different powers

Lin-jiang CHAI[1], Shan-shan YUAN[1], Wei-jiu HUANG[1],
Xu-sheng YANG[1], Fang-jun WANG[2], Dong-zhe WANG[2], Jun-jun WANG[1]

1. College of Materials Science and Engineering, Chongqing University of Technology, Chongqing 400054, China;
2. Chongqing Materials Research Institute Co., Ltd., Chongqing 400707, China

Received 3 September 2017; accepted 15 April 2018

Abstract: An annealed Inconel 718 alloy was surface-treated by pulsed laser at three different powers (100, 50 and 25 W). Microstructural changes induced by the laser treatments were characterized by use of electron backscatter diffraction and electron channeling contrast imaging techniques. Results show that both annealing twins and strengthening precipitates profusely existing in the as-received specimen are dissolved at elevated temperatures during the laser irradiation. Meanwhile, in the melting zone (MZ), densities of low angle boundaries (LABs) are greatly increased with a large number of Laves phases preferentially distributed along such LABs. For different specimens, widths and depths of their MZs are found to be gradually reduced with decreasing the laser powers. Orientation analyses reveal that the columnar grains in the MZ of the 100 W specimen could inherit orientations existing in the matrix while lower laser powers promote the formation of more nuclei with scattered orientations to grow to be granular grains in the MZ. Hardness tests reveal that the MZs of all laser-treated specimens are softer than the matrix probably due to both precipitate dissolution and grain coarsening.

Key words: Inconel 718 alloy; grain boundaries; pulsed laser surface treatment; electron backscatter diffraction; hardness

1 Introduction

As a nickel base superalloy, Inconel 718 alloy has wide application in nuclear, aeronautics and power industries thanks to many attractive properties like satisfactory corrosion resistance and superior mechanical properties at high temperature up to 650 °C [1−4]. However, fretting wear occasionally appears on the surface due to the interfacial debonding of carbide compounds (NbC) with the Nb segregation when the temperature approaches 1050 °C [5,6]. These precipitates usually lead to premature failures of components and thus affect the surface mechanical properties. To date, various techniques have been attempted for Inconel 718 alloy to obtain optimized surface properties. Among them, laser surface treatment was reported to own many advantages such as operation precision and efficiency without modifying the alloy bulk properties [7,8]. Specifically, laser surface processing can selectively heat and even melt a narrow volume, accompanied by the formation of large temperature gradient and high thermal stress fields. It was reported that significant microstructural and property modifications could be reached after laser-related processing. TUCHO et al [9] reported that grain structures of selective laser melted Inconel 718 specimens were generally separated by sub-grain boundaries and high density of dislocation networks. PARIMI et al [10] attempted to characterize microstructures and textures of Inconel 718 prepared by the direct laser fabrication method and found that columnar grain structures with a ⟨001⟩ fiber texture could be formed using a high laser power input. Stress analyses for the laser-modified zones of Inconel 718 alloy were recently performed by YILBAS et al [11] and they found that the maximum value of residual stress could be close to the yielding limit of the alloy.

In spite of the above results documented for laser-treated nickel base superalloys, attention paid to their microstructural characteristics remains to be rather

---

Foundation item: Project (CSTC2015ZDCY-ZTZX50002) supported by the Innovation Program of Common and Key Technologies in Major Industries of Chongqing, China

Corresponding author: Wei-jiu HUANG; Tel: +86-23-62408527; E-mail: huangweijiu@cqut.edu.cn

DOI: 10.1016/S1003-6326(18)64794-6

limited, compared with efforts made for other metallic materials [12−16]. In the present study, therefore, laser surface treatments at three different powers were carried out for an Inconel 718 superalloy, with detailed microstructures in the laser-modified zones characterized by electron backscatter diffraction (EBSD) and electron channeling contrast (ECC) imaging techniques. Hardness measurements were also made for the laser-treated specimens. Results presented in this work are expected to facilitate better understanding on effects of laser surface treatments on the nickel base superalloy.

2 Experimental

The as-received Inconel 718 material was a *d*20 mm rod after solution heat treatment at 720 °C for 8 h and aging treatment at 620 °C for 8 h, with its chemical composition listed in Table 1. Rectangular specimens with dimensions of 15 mm × 10 mm × 3 mm along three orthogonal directions (namely rolling direction (RD), transverse direction (TD) and normal direction (ND), respectively) were cut from the as-received material. RD−TD surfaces of the specimens were irradiated by a pulsed laser device (600W Nd: YAG) at three different powers (100, 50 and 25 W), with detailed processing parameters listed in Table 2.

Table 1 Chemical composition of Inconel 718 material (mass fraction, %)

Ni	Cr	Fe	Nb	Mo
52.6	18.91	18.63	5.03	3.2
Ti	Al	Si	Mn	P
1.03	0.51	0.075	0.015	0.006

By use of ECC imaging and EBSD techniques in a Zeiss Sigma HD field emission scanning electron microscope (FEG-SEM), RD−ND planes of the laser-treated specimens were carefully examined to reveal their microstructural characteristics. High-quality ECC images have been manifested to be capable of well revealing morphologies of (sub-)grains and structural defects like precipitates and twins in various metallic materials [12,13,16]. Crystallographic orientations corresponding to those microstructural features could be further investigated quantitatively by the EBSD technique. The EBSD system attached to the FEG-SEM comprised an Oxford Instruments NordlysMax^2 detector and AZtec 2.4 software for data acquisition, with an HKL Channel 5 software package used for data post processing analyses. Before ECC and EBSD examinations, the to-be-analyzed planes were mechanically ground using SiC abrasive papers and then electro-polished in a mixed solution of 10% perchloric acid and 90% (volume fraction) ethyl alcohol at 30 V and −30 °C for about 1 min.

Micro hardnesses of the Inconel 718 superalloy were also measured for the laser surface-treated specimens using a Vickers indentation tester (HVS−1000). The hardness indentations were made across the laser-modified zones at an interval of 200 μm and a load of 100 g. For each specimen, more than ten indentations were made along each measuring path and such measurements were repeated at least five times.

3 Results and discussion

3.1 Starting microstructure

Figure 1 shows microstructural characteristics of the as-received material (before the laser surface treatment) revealed by ECC and EBSD techniques. Clearly, the microstructures consist of equiaxed austenitic grains and numerous second phase particles (SPPs) which are mainly distributed along grain boundaries. The average size of the equiaxed grains is measured to be about 7.3 μm. Direct observation from Fig. 1(a) reveals many annealing twins that divide their parent grains by straight boundaries. A boxed region in Fig. 1(a) is magnified in Fig. 1(b), from which one can see that a few SPPs also appear in grain interiors. In Inconel 718 alloys, main strengthening phases contain three types: γ'' (Ni_3Nb), γ' ($Ni_3(Al,Ti)$) and δ (Ni_3Nb). The γ'' and γ' are the primary and the secondary precipitation strengthening phases, respectively. The δ precipitate is the equilibrium substitution of the metastable γ'' phase. According to earlier works [17−20], morphologies of these strengthening phases would vary a lot at different temperatures. The γ'' phase with the sphere shape exists in the temperature range of 600−900 °C while the δ phase with the long needle shape often appears in the temperature range of 750−1020 °C [15]. Morphologically, it is hard to differentiate the γ' phase

Table 2 Processing parameters of pulsed laser surface treatments

Scanning velocity/ ($mm\cdot s^{-1}$)	Laser power/W	Beam diameter/mm	Pulse duration/ ms	Pulse frequency/ Hz	Power density/ ($W\cdot mm^{-2}$)	Energy density/ ($J\cdot mm^{-1}$)
8	25	2	2.5	20	31.85	3.13
8	50	2	5	20	63.7	6.25
8	100	2	5	20	127.4	12.5

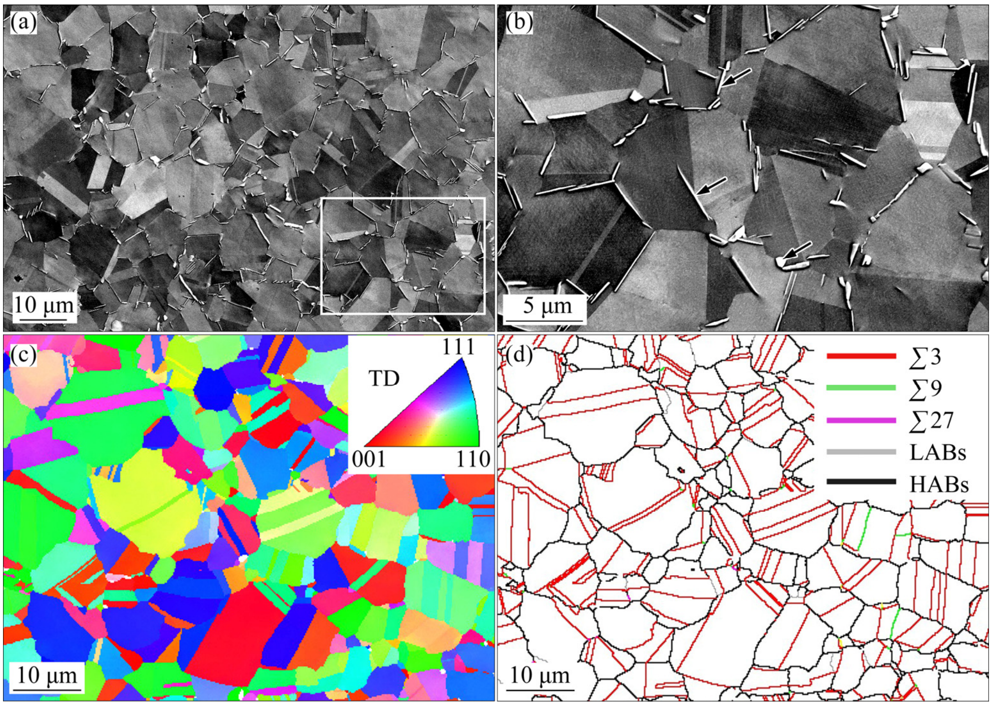

Fig. 1 ECC (a, b) and EBSD (c, d) maps (step size 0.2 μm) of as-received specimens

from the γ'' phase. Thus, the annealing condition of 720 °C for 8 h for the initial specimen is thought to be insufficient to dissolve the strengthening phases. In Fig. 1(b), the long needle phases and the short rod/granular precipitates are believed to be δ and γ'' phases, respectively, as indicated by black arrows. These dispersed phases could impede dislocation movements during deformation, leading to a precipitation hardening effect.

Figures 1(c) and (d) are EBSD inverse pole figure (IPF) and grain boundary (GB) map of the as-received specimen. Grain orientations are colored according to the standard triangle inset in Fig. 1(c) and the varying colors represent different crystal orientations. It is noticed that orientations of the grains are rather scattered in this map, indicating the absence of a crystallographic texture.

Special coincident site lattice (CSL) boundaries with $\Sigma 3^n$ ($1 \le n \le 3$), along with random high angle boundaries (HABs, $\theta > 15°$) and low angle boundaries (LABs, $2° < \theta < 15°$), are presented in Fig. 1(d). Such a map is able to reveal connectivity of the grain boundary network [21]. It can be observed from Fig. 1(d) that the type of $\Sigma 3$ boundary is the most dominant one. Earlier studies indicated that $\Sigma 3$ boundaries had low interface energies and could thus be readily generated by virtue of twin events [22−25].

3.2 Microstructures after laser surface treatments

Cross-sectional views of microstructures in the laser-treated specimens are exhibited in Fig. 2. The irradiated zones and the substrate are found to have distinct morphologies. The melting zones (MZs) in all the specimens show bowl-like morphologies, as indicated by the dashed lines. For the 100 W specimen,

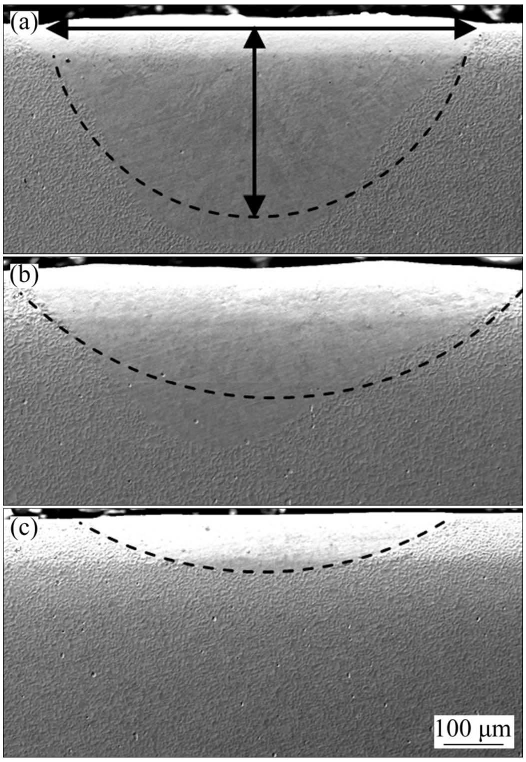

Fig. 2 Cross-sectional observations of laser surface-treated specimens at different powers: (a) 100 W; (b) 50 W; (c) 25 W (Dashed lines roughly outline the melting zones with measuring ranges of their widths and depths schematically indicated by double-arrow lines in (a))

the maximum width and depth of its MZ are measured to be about 850 and 420 μm, respectively. For specimens laser-treated at lower powers, the maximum widths and depths of their MZs are found to be reduced, i.e., 780 μm and 270 μm for the 50 W specimen and 690 μm and 110 μm for the 25 W specimen, respectively. The smaller MZs could be ascribed to lower energy input and thus easier heat extraction by the substrate in the 50 W and 25 W specimens.

Figure 3 presents ECC observations for the laser-modified zones in various specimens. Coarse columnar grains (hundreds of micrometers in length and tens of micrometers in width) can be seen in the MZ of the 100 W specimen (Fig. 3(a)), with their long axes towards the laser beam center. These columnar grains are believed to result from the melt solidification during the laser irradiation. Inside them, there exist a large number of SPPs with morphologies distinctly different from those observed in the as-received specimen. These SPPs have an average size of (90±25) nm and a net-like distribution, as clearly shown in Fig. 3(b). In the specimens with lower laser powers (25 and 50 W), the solidified grains seem to be more granular with dense SPPs in their interiors as well (Figs. 3(c) and (e)). Morphologies, sizes and densities of those SPPs are found to be similar in all the laser-treated specimens. Nevertheless, with decreasing laser powers, it seems that their network distribution tends to change to be band-like distribution (Figs. 3(b), (d) and (f)). Previous studies showed that the highest temperature during the laser surface treatment of nickel base alloy would be easily above 1100 °C [7]. However, the main strengthening phases in the Inconel 718 alloy will be fully dissolved in the temperature range of 950−1020 °C. Since *γ*-type and *δ* precipitates are no longer detected in the laser-modified zones in the present work, one could deduce that they are dissolved at elevated temperatures. In fact, such net-like or band-like distributed SPPs have been well characterized and determined to be Laves phases in earlier works [9,10,17]. Note that the Laves phases were reported to be detrimental to the mechanical properties [9,26].

EBSD maps revealing the orientation-related microstructural features of the 100 W specimen are

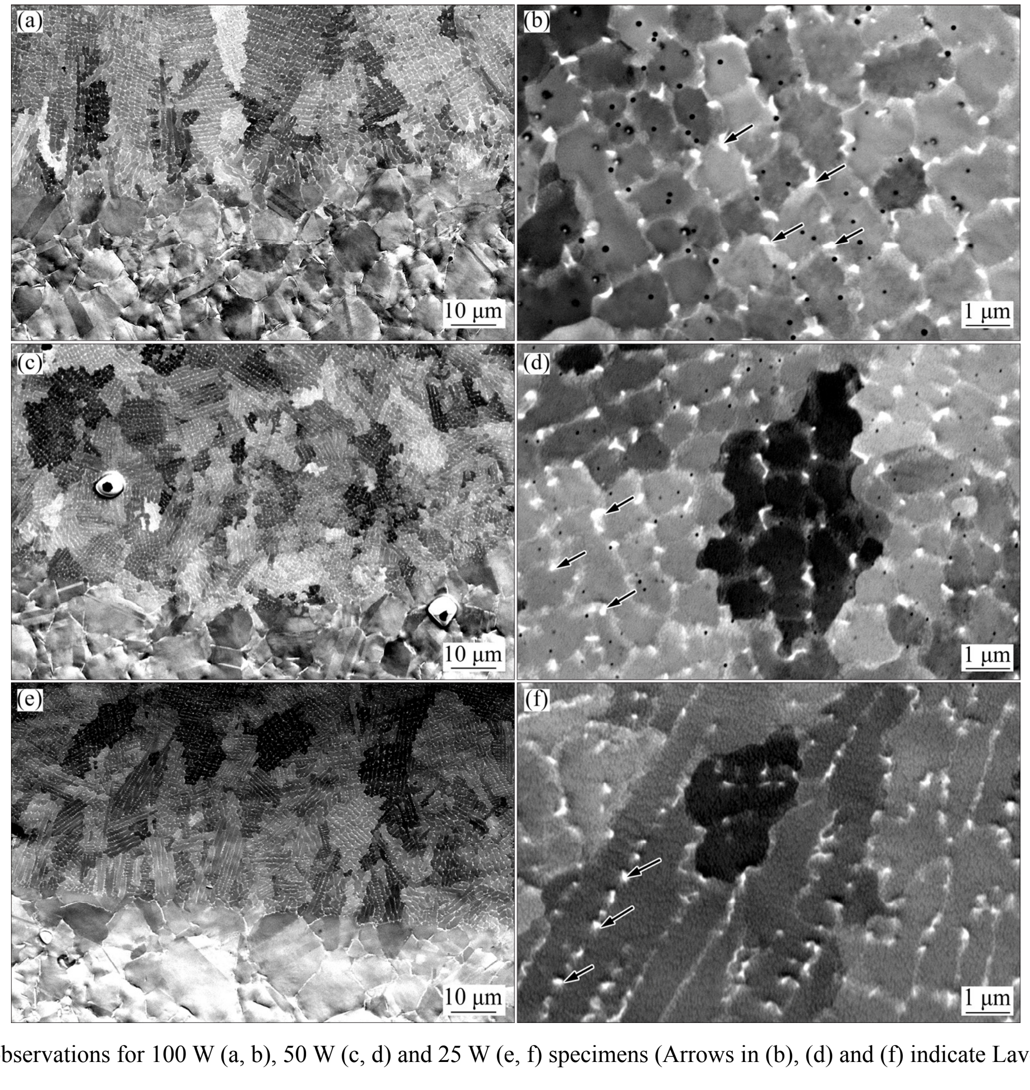

Fig. 3 ECC observations for 100 W (a, b), 50 W (c, d) and 25 W (e, f) specimens (Arrows in (b), (d) and (f) indicate Laves phases)

shown in Fig. 4. From Fig. 4(a), the irradiated region and the substrate can also be roughly distinguished, as indicated by the black dashed lines. The average grain size measured for the laser-modified zone in the specimen is about 9.3 μm, larger than that of the substrate (7.3 μm). In the MZ, the grain orientations are noticed to be still scattered (Fig. 4(b)). In the earlier work, YILBAS et al [11] performed a systematic study on temperature prediction in laser-irradiated region using the finite element method. They concluded that the temperature variation around the laser beam intensity distribution along the RD was low during heating and became high in the cooling period after the melting initiation. This suggested that the temperature was higher near the surface than around the bottom of the MZ and gradually decreased from the laser beam center to regions far away. As the pulse duration is very short in the present work, sufficient heat extraction through the cold substrate could lead to a remarkable self-quenching effect. The formation of columnar structures should be related to preferable growth of nuclei in the melt along the direction of temperature gradient decrease. Besides, the presence of many LABs indicates a high density of entangled dislocations. Such dislocation structures are believed to be induced by accumulated thermal stresses during the laser treatment. The dislocation networks could impede subsequent dislocation movements across cellular microstructure, as reported by LIN et al [27].

In regards to profuse annealing twins existing in the as-received material, careful microstructural observation suggests their disappearance in the laser-modified zones. It is known that sufficient boundary migration is usually needed for the formation of annealing twins [25]. However, in the laser-modified zone, rapid solidification occurs so that such twins could not be developed due to limited time for diffusion.

A similar analysis to Fig. 4 was also made for the 50 W specimen, as presented in Fig. 5. As already

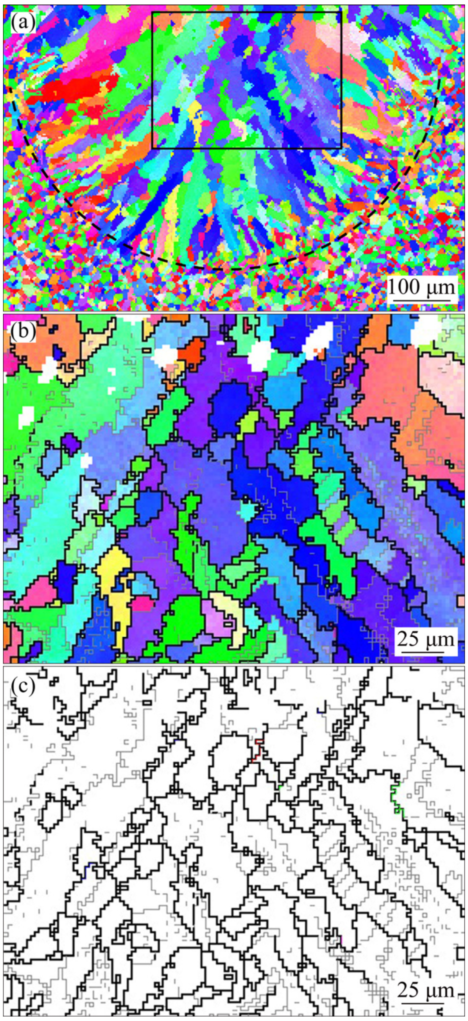

Fig. 4 EBSD IPF map (step size 2 μm) for laser-modified zone of 100 W specimen (dashed line roughly outlines melting zone) (a), and enlarged maps (b, c) of boxed region in (a) with black and gray lines indicating HABs and LABs, respectively

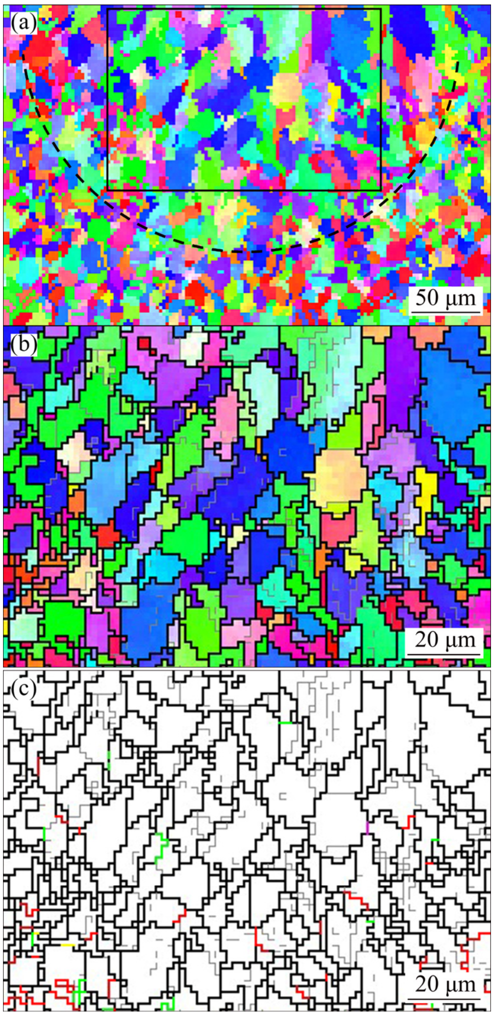

Fig. 5 EBSD IPF map (step size 2 μm) for laser-modified zone of 50 W specimen (dashed line roughly outlines melting zone) (a) and enlarged maps (b, c) of boxed region in (a) with black and gray lines indicating HABs and LABs, respectively

noticed in Fig. 2, the MZ of the 50 W specimen is smaller than that of the 100 W specimen. Along with the reduced laser-modified volume, grains in the MZ of the 50 W specimen are also found to be slightly refined. This may be attributed to the lower temperature and the higher cooling rate induced by the lower laser power, leading to suppressed grain growth [28]. For the specimen laser-treated at even lower power (25 W), its main microstructural features greatly resemble those revealed for the 50 W specimens, except a further refined grain structure (not shown here).

To better probe the misorientation characteristics of the laser-modified zones in the 100 W and the 50 W specimens, their misorientation histograms are compared with that of the substrate. From Fig. 6(a), one can see that an evident peak around 60° with a rotation axis focused on ⟨111⟩. Such a 60°/⟨111⟩ misorientation is known to correspond to the annealing twin relationship ($\Sigma 3$) in face centered cubic metals. This result is in a good agreement with that observed in Fig. 1(d), confirming the abundance of annealing twins in the as-received Inconel 718 alloy. After laser surface treatments, however, Figs. 6(b) and (c) reveal that the 60° peak is greatly suppressed, consistent with the disappearance of annealing twins by microstructural observation (Figs. 4(b) and 5(b)). In contrast, the fraction of low misorientation angles (<15°) is evidently increased in the laser-modified zones, much higher than that of the substrate. As above mentioned, these LABs should be aroused by laser-induced thermal stresses.

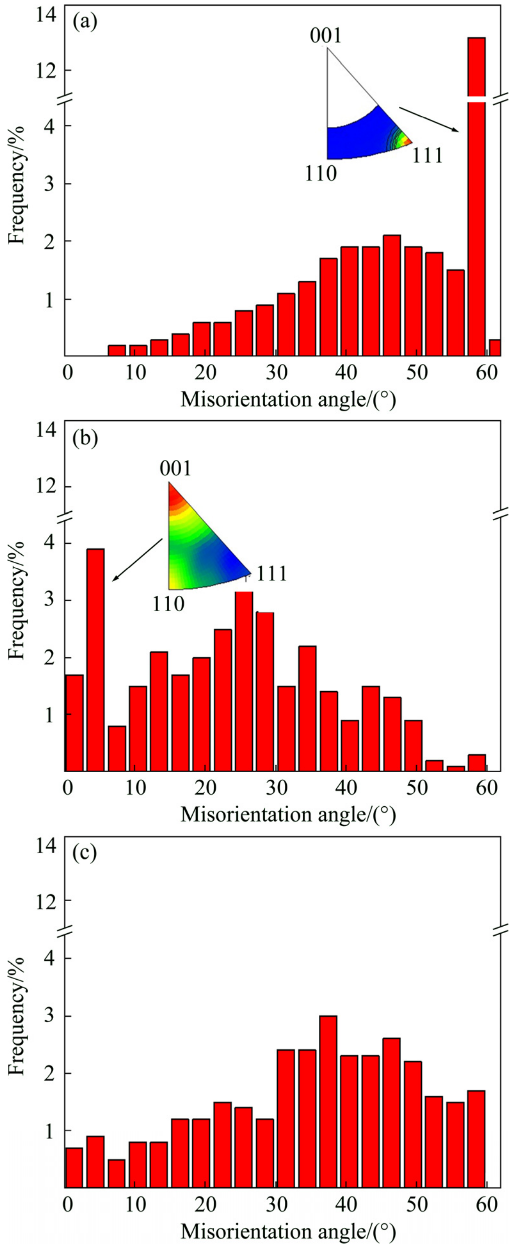

Fig. 6 Misorientation angle distribution histograms of as-received (a), 100 W (b) and 50 W (c) specimens, corresponding to EBSD data in Figs. 1(c), 4(b) and 5(b), respectively

Since the EBSD technique allows orientations of both the MZ and the substrate to be simultaneously obtained, the orientation relationship between them could then be analyzed (Fig. 7). Figure 7(a) shows an ECC image covering a few columnar grains in the laser-modified zone of the 100 W specimen and several neighboring equiaxed grains belonging to the substrate. Figures 7(b) and (c) show IPF and GB maps roughly corresponding to Fig. 7(a). Close observation reveals that the columnar grains at the bottom of the MZ prefer to inherit orientations of some equiaxed grains in the substrate (Figs. 7(b) and (c)). For example, along the arrows 1 and 2, uniform orientations corresponding to parts of both columnar and equiaxed grains can be clearly seen. Such results suggest that the columnar grains in the MZ should have nucleated by relying on some equiaxed grains so that the existing orientations were inherited in an epitaxial growth way. For specimens with lower laser powers, the columnar grains are replaced by more granular grains in the MZs (Fig. 3) and the epitaxial growth of existing orientations is not noticed (Fig. 5). Smaller melting pools (Fig. 2) are produced with decreasing laser powers which lead to higher cooling rates due to easier heat dissipation. As a result, this could produce a larger undercooling and thus more nuclei in the melt. In contrast with the preference of columnar grains in the 100 W specimen, the presence of abundant nuclei can grow to be more granular grains with random orientations in the 25 W and the 50 W specimens.

3.3 Hardness variation

In addition to the microstructural characteristics as detailed above, hardness tests for the laser-treated specimens are given in Fig. 8. An example illustrating sites and morphologies of the hardness indentations made on a laser-scanned surface is shown in Fig. 8(a). Generally, as indicated by the varying indentation sizes, the substrate seems to be harder than the laser

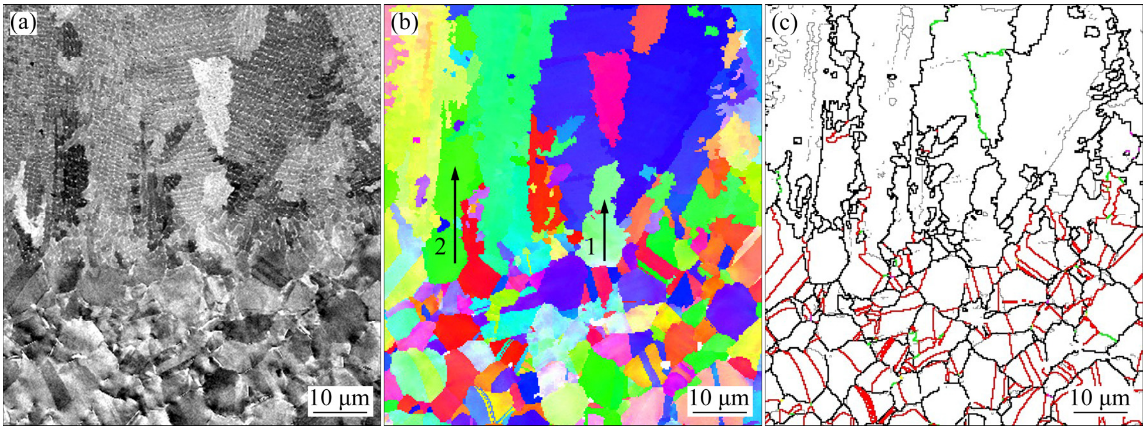

Fig. 7 Illustration of grain orientation relationship between melting zone and substrate of 100 W specimen: (a) ECC; (b) IPF; (c) GB map (step size 0.3 μm)

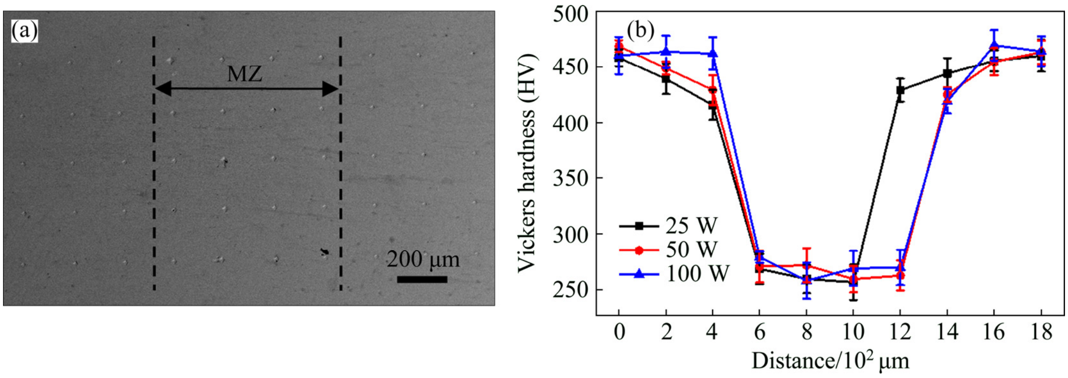

Fig. 8 Surface hardness variation across laser-modified zones in laser-treated specimens: (a) Indentation sites and morphology; (b) Variation of hardness (Dashed lines in (a) roughly distinguish the laser-modified zone and the matrix)

surface-treated zones. Measurements show that the hardness of the substrate is HV (440±10). For all the three laser-treated specimens, the MZs near the beam center seem to be the softest locations. The lowest hardness value is HV (275±20), keeping stable with the change of laser powers. Thus, there is a near 40% hardness drop after the laser treatments.

Main reasons for the softening of the MZ are tentatively analyzed as follows. Firstly, the strengthening SPPs including γ'', γ' and δ phases in the as-received material (the substrate) are dissolved in the laser-treated regions. Therefore, the prior strengthening effect due to SPPs is removed. Secondly, the columnar/granular grains in the MZs are coarser than the initial equiaxed grains, leading to weaker hardening of grain boundaries. Although more LABs are produced after the laser treatments, their impedance to dislocation movements seems to be limited.

4 Conclusions

1) For specimens laser-treated at different powers, widths and depths of their MZs are gradually reduced with decreasing laser powers.

2) After being pulsed laser treatments, annealing twins profusely existing in the as-received material were absent in the MZs, with many LABs appearing due to the accumulated thermal stresses.

3) Columnar grains formed in the MZ of the 100 W specimen could inherit orientations existing in the matrix, while decreased laser powers promote the formation of more nuclei with scattered orientations to grow to be granular grains.

4) The dissolution of the strengthening phases and the coarsened grain structures jointly lead to decreased hardness in the MZ.

References

[1] FU S H, DONG J X, ZHANG M C, XIE X S. Alloy design and development of Inconel 718 type alloy [J]. Materials Science and Engineering A, 2009, 499(1−2): 215−220.

[2] MIGNANELLI P M, JONES N G, PERKINS K M, HARDY M C, STONE H J. Microstructural evolution of a delta containing nickel-base superalloy during heat treatment and isothermal forging [J]. Materials Science and Engineering A, 2015, 621: 265−271.

[3] KIRKA M M, MEDINA F, DEHOFF R, OKELLO A. Mechanical behavior of post-processed Inconel 718 manufactured through the

electron beam melting process [J]. Materials Science and Engineering A, 2017, 680: 338−346.

[4] LIU T, XIA S, LI H, ZHOU B, BAI Q. Effect of the pre-existing carbides on the grain boundary network during grain boundary engineering in a nickel based alloy [J]. Materials Characterization, 2014, 91: 89−100.

[5] LIN Y C, DENG J, JIANG Y Q, WEN D X, LIU G. Hot tensile deformation behaviors and fracture characteristics of a typical Ni-based superalloy [J]. Materials & Design, 2014, 55: 949−957.

[6] LONG Yi-tong, NIE Pu-lin, LI Zhu-guo, HUANG Jian, LI Xiang, XU Xin-mei. Segregation of niobium in laser cladding Inconel 718 superalloy [J]. Transactions of Nonferrous Metals Society of China, 2016, 26(2): 431−436.

[7] YILBAS B S, ALI H, ALAQEELI N, KARATAS C. Laser treatment of Inconel 718 alloy and surface characteristics [J]. Optics & Laser Technology, 2016, 78: 153−158.

[8] LIU L, HIROSE A, KOBAYASHI K F. A numerical approach for predicting laser surface annealing process of Inconel 718 [J]. Acta Materialia, 2002, 50: 1331−1347.

[9] TUCHO W M, CUVILLIER P, SJOLYST-KVERNELAND A, HANSEN V. Microstructure and hardness studies of Inconel 718 manufactured by selective laser melting before and after solution heat treatment [J]. Materials Science and Engineering A, 2017, 689: 220−232.

[10] PARIMI L L, RAVI G A, CLARK D, ATTALLAH M M. Microstructural and texture development in direct laser fabricated IN718 [J]. Materials Characterization, 2014, 89: 102−111.

[11] YILBAS B S, AKHTAR S S, KARATAS C. Laser surface treatment of Inconel 718 alloy: Thermal stress analysis [J]. Optics & Lasers in Engineering, 2010, 48(7−8): 740−749.

[12] CHAI L, WANG S, WU H, GUO N, PAN H, CHEN L, MURTY K L, SONG B. $\alpha \to \beta$ Transformation characteristics revealed by pulsed laser-induced non-equilibrium microstructures in duplex-phase Zr alloy [J]. Science China Technological Sciences, 2017, 60: 1255−1262.

[13] CHAI L, WU H, ZHENG Z, GUAN H, PAN H, GUO N, SONG B, Microstructural characterization and hardness variation of pure Ti surface-treated by pulsed laser [J]. Journal of Alloys and Compounds, 2018, 741: 116−122.

[14] ZHOU Zhi-ming, CHAI Lin-jiang, XIAO Zhi-pei, TU Jian, WANG Ya-ping, HUANG Wei-jiu. Surface modification of Cu−25Cr alloy induced by high current pulsed electron beam [J]. Transactions of Nonferrous Metals Society of China, 2015, 25(6): 1935−1943.

[15] KOPPOJU S, SHARIFF S M, SINGH A K, MANTRIPRAGADA R, GADHE P, JOSHI S V. Evolution of texture during laser surface treatment of an austenitic manganese steel [J]. Materials Characterization, 2015, 102: 29−34.

[16] CHAI L, WU H, WANG S, CHEN K, WANG T, XIA J. Characterization of microstructure and hardness of a Zr−2.5Nb alloy surface-treated by pulsed laser [J]. Materials Chemistry and Physics, 2017, 198: 303−309.

[17] COZAR R, PINEAU A. Morphology of γ' and γ precipitates thermal stability of Inconel 718 type alloy [J]. Metallurgical Transactions, 1973, 4: 47−49.

[18] CAI D, ZHANG W, NIE P, LIU W, YAO M. Dissolution kinetics of δ phase and its influence on the notch sensitivity of Inconel 718 [J]. Materials Characterization, 2007, 58 (3): 220−225.

[19] CIESLAK M J, KNOROVSKY G A, HEADLEY T J, ROMIG A D. Inconel 718: A solidification diagram [J]. Metallurgical Transactions A, 1987, 20: 1989−2149.

[20] DENG De-wei, WANG Chun-guang, LIU Qian-qian, NIU Ting-ting. Effect of standard heat treatment on microstructure and properties of borided Inconel 718 [J]. Transactions of Nonferrous Metals Society of China, 2015, 25 (2): 437−443.

[21] HOU G, LUO H, LV J, Grain boundary character distribution and sensitisation behaviour of grain boundary engineered stable austenitic stainless steel (AISI 316L) [J]. Materials Science and Technology, 2014, 30(12): 1447−1452.

[22] RANDLE V. Twinning-related grain boundary engineering [J]. Acta Materialia, 2004, 52 (14): 4067−4081.

[23] THOMSON C B, RANDLE V. “Fine tuning” at $\Sigma 3^n$ boundaries in nickel [J]. Acta Metallurgica, 1997, 45: 4909−4916.

[24] XIA S, ZHOU B X, CHEN W J, WANG W G. Effects of strain and annealing processes on the distribution of $\Sigma 3$ boundaries in a Ni-based superalloy [J]. Scripta Materialia, 2006, 54(12): 2019−2022.

[25] BAIR J L, HATCH S L, FIELD D P. Formation of annealing twin boundaries in nickel [J]. Scripta Materialia, 2014, 81: 52−55.

[26] QU F S, LIU X G, XING F, ZHANG K F. High temperature tensile properties of laser butt-welded plate of Inconel 718 superalloy with ultra-fine grains [J]. Transactions of Nonferrous Metals Society of China, 2012, 22 (10): 2379−2388.

[27] LIN Y C, LI L, HE D G, CHEN M S, LIU G Q. Effects of pre-treatments on mechanical properties and fracture mechanism of a nickel-based superalloy [J]. Materials Science and Engineering A, 2017, 679: 401−409.

[28] LIU H, NAKATA K, ZHANG J X, YAMAMOTO N, LIAO J, Microstructural evolution of fusion zone in laser beam welds of pure titanium [J]. Materials Characterization, 2012, 65: 1−7.

不同功率下脉冲激光表面处理 Inconel 718 合金的显微组织

柴林江[1]，袁珊珊[1]，黄伟九[1]，杨绪盛[1]，王方军[2]，王东哲[2]，王军军[1]

1. 重庆理工大学 材料科学与工程学院，重庆 400054；2. 重庆材料研究院有限公司，重庆 400707

摘 要：对退火态的 Inconel 718 合金进行 3 种不同功率(100、50 和 25 W)的脉冲激光表面处理，并应用电子背散射衍射和电子通道衬度成像技术对其表面显微组织特征进行研究。结果表明，激光表面处理导致所制备的样品中大量存在的退火孪晶和强化析出相消失；同时，激光重熔区中出现许多小角度晶界，且沿着这些晶界存在高密度的 Laves 相。随着激光功率的降低，样品重熔区的宽度和深度均逐渐变小。取向分析表明，100 W 样品激光重熔区中的柱状晶可通过取向形核机制遗传初始组织的随机取向，而降低激光功率会促使重熔区中产生大量具有随机取向的晶核，它们最终长成等轴晶。硬度测试发现所有样品的激光重熔区均较基体软，这主要与强化相的溶解和晶粒的粗化有关。

关键词：Inconel 718 合金；晶界；脉冲激光表面处理；电子背散射衍射；硬度

(Edited by Xiang-qun LI)